RESEARCH ARTICLE

TITLE: H^+/K^+ ion pump enhances cytoskeletal polarity to drive gastrulation in sea urchin embryo

Running title: H^+/K^+ ion pump and gastrulation

Kaichi Watanabe[1,*], Yuhei Yasui[1], Yuta Kurose[2], Masashi Fujii[1], Takashi Yamamoto[1], Naoaki Sakamoto[1,*], Akinori Awazu[1,3,*]

[1] Graduate School of Integrated Sciences for Life, Hiroshima University, Higashi-Hiroshima, 739-8526, Japan

[2] Department of Mathematical and Life Sciences, Graduate School of Science, Hiroshima University, Higashi-Hiroshima, 739-8526, Japan

[3] Research Center for the Mathematics on Chromatin Live Dynamics, Hiroshima University, Higashi-Hiroshima, Hiroshima, 739-8526, Japan

*Corresponding authors (kaichi1849@hiroshima-u.ac.jp (K.W.); naosaka@hiroshima-u.ac.jp (N. S.); awa@hiroshima-u.ac.jp (A. A.))

KEY WORDS: Gastrulation, H^+/K^+ ion pump, sea urchin, cytoskeleton, pH regulation

Summary statement: The H^+/K^+ ion pump is critical for normal gastrulation in sea urchin through pH regulation of cell-position dependent intracellular actin distributions.

ABSTRACT

Gastrulation is a universal process in the morphogenesis of many animal embryos. In sea urchin embryos, it involves the invagination of single-layered vegetal plate into blastocoel. Although morphological and molecular events have been well studied for gastrulation, the mechanical driving forces and their regulatory mechanism underlying the gastrulation is not fully understood. In this study, structural features and cytoskeletal distributions were studied in sea urchin embryo using an "exogastrulation" model induced by inhibiting the H^+/K^+ ion pump with omeprazole. The vegetal pole sides of the exogastrulating embryos had reduced roundness indices, intracellular pH polarization, and intracellular F-actin polarization at the pre-early gastrulation compared with the normal embryo. Gastrulation stopped when F-actin polymerization or degradation was inhibited by *RhoA* or *YAP1* knockout, although pH distributions were independent of such a knockout. A mathematical model of sea urchin embryos at the early gastrulation reproduced the shapes of both normal and exogastrulating embryos using cell-dependent cytoskeletal features based on F-actin and pH distributions. Thus, gastrulation required appropriate cell position-dependent intracellular F-actin distributions regulated by the H^+/K^+ ion pump through pH control.

41 **INTRODUCTION**

42 Gastrulation is a universal and essential morphogenic process in various animals,
43 wherein a ball of single layered cells (blastula) differentiates into a multilayered
44 gastrula or early embryo (Serrano Nájera and Weijer, 2020; Shindo, 2018; Stower and
45 Bertocchini, 2017). Species-specific variations in this process provides the basis for
46 particular animal morphologies and leads to the generation of internal organs. The basic
47 mechanism of whole embryonic transformations induced by organizational
48 rearrangements and cell movements are expected to be universal.

49 Sea urchin embryos are commonly used for studying various morphogenetic
50 processes universally observed in animals, such as the left–right symmetry breakage
51 (Aihara and Amemia, 2001; McCain and McClay, 1994; Takemoto et al., 2016; Warner
52 and McClay, 2014), neural network formations (Burke et al., 2014; McClay et al., 2018;
53 Yaguchi et al., 2010), and gastrulation (Dan and Okazaki, 1956; Gustafson and
54 Kinnander, 1960; Hardin and Cheng, 1986; Kominami and Takata, 2004; Martik and
55 McClay, 2017) due to its evolutionary position as an ancestral deuterostome.
56 Furthermore, the gene regulatory network controlling endomesoderm specification in
57 sea urchin embryo has been well studied (Davidson et al., 2002; Oliveri & Davidson,
58 2004). Sea urchin gastrulation progresses through the following four steps (Kominami
59 and Takata, 2004): step 1 (after hatching), the embryo becomes an epithelial monolayer
60 with a thickened vegetal pole; step 2 (pre-gastrulation), the vegetal plate bends to
61 invade the blastocoel; step 3 (early gastrulation), the tubular archenteron is formed, and
62 secondary mesenchyme cells (SMCs) appear at the tip; step 4 (mid-late gastrulation),

63 the archenteron elongates by pulling on the filopodia of the SMC. Steps 1 and 2 refer to
64 the primary invagination stages, and steps 3 and 4 are those of the secondary
65 invagination stages (Dan and Okazaki, 1956; Gustafson and Kinnander, 1956).
66 The embryos of some sea urchin species exhibit anomalous morphogenesis
67 (exogastrulation) under various perturbations where the vegetal plate of the embryo
68 prolapses outward instead of invaginating. For example, the archenteron of embryos
69 cultured with LiCl or sugar is completely evaginated due to the depolymerization of
70 SMC microtubules in the blastocoel space connecting the primary intestine and
71 ectoderm (Dan and Okazaki, 1956; Hardin and Cheng, 1986; Khurrum et al., 2004).
72 These studies suggest that lifting the primary intestine from the mid-gut by
73 microtubules plays an important role in step 4 of gastrulation. Exogastrulation was also
74 observed by Rab35 knockdown that was also suggested to disturb whole embryonic
75 cytoskeleton distribution (Remsburg et al., 2021).
76 Moreover, bending of the vegetal plate in step 2 of normally cultured embryos of
77 the sea urchin, *Lytechinus pictus* (LP), occurs even when it is surgically isolated
78 (Ettensohn, 1984). It is suggested that the tip of the archenteron should be bottle-shaped
79 (Nakajima and Burke, 1996), and the area around the vegetal plate should be wedge-
80 shaped (Burke et al., 1991) to initiate primary invagination (Kominami and Takata,
81 2004). Additionally, mathematical models of vegetal poles suggest that primary
82 invagination occurs under the appropriate force conditions for “apical constriction,”
83 “cell tractor,” “apical contractile ring,” “apicobasal contraction,” and “gel swelling”
84 (Davidson et al., 1995; Odell et al., 1981). However, it is unclear which of these effects

are essential for development up to pre-early gastrulation (steps 2 and 3).

In this study, the roles of the dominant factors in steps 2 and 3 of gastrulation of sea urchins were determined through experimental analyses and mathematical modeling. First, specific inhibition of H^+/K^+ ion pump activity by omeprazole caused "partial" exogastrulation without the loss of microtubules in the blastocoel space of embryos from the sea urchin, *Hemicentrotus pulcherrimus* (HP). The H^+/K^+ ion pump regulates the pH in cells and pH influences the structure and force of the actomyosin system (Köhler et al., 2012). Therefore, the partial exogastrulation was likely due to anomalous cytoskeletal behaviors. Second, knockout experiments on cytoskeleton-related molecules were performed in HP embryos and analyzed by fluorescence imaging. Third, simulations of morphogenic process of normal and H^+/K^+ ion pump inhibited (exhibiting exogastrulation) HP embryo during the pre-early gastrulation were performed using a mathematical model utilizing the cytoskeletal force parameters determined by the above experiments. The modeled shapes of the H^+/K^+ ion pump-inhibited embryos of the sea urchin, *Lytechinus variegatus* (LV,) were compared to those of HP to reveal the contributions of the H^+/K^+ ion pump to the regulation of cytoskeletal behaviors.

RESULTS

H^+/K^+ ion pump inhibition in HP embryos caused partial exogastrulation

The development of HP embryos exposed to the specific H^+/K^+ ion pump inhibitor, omeprazole, immediately after fertilization exhibited anomalous morphogenesis with

107 partial exogastrulation observed at the primary-secondary invagination stages and 36
108 hours post fertilization (hpf) (Fig. 1). Detailed comparisons of the structural features
109 around the vegetal pole between the normal (control) and inhibited embryos at each
110 gastrulation step are as follows. In step 1, control and inhibited embryos exhibited
111 equivalent vegetal pole thickening (18-20 hpf). In step 2, primary invagination occurred
112 in both control and inhibited embryos at the same time. However, intestinal invagination
113 was slightly shallower in the inhibited embryos than in the control embryos (20-22 hpf).
114 In step 3, inhibited embryos did not show further elongation of the archenteron into the
115 blastocoel, and the shape of inhibited embryos elongated along the animal-vegetal axis
116 (22-24 hpf). In step 4 (secondary invagination stage), the outward protrusion of the
117 vegetal pole side was more pronounced in the inhibited embryo (24 hpf). The inhibited
118 embryo had comparatively little elongation of the archenteron into the blastocoel
119 compared to the control embryos. At 36 hpf, "partial" exogastrulation, in which the tip
120 of archenteron folded inward by the normal primary invagination but the remaining part
121 extended outward during the secondary invagination, was observed in the inhibited
122 embryo.
123 The migration of SMCs was observed in the control embryos and in the inhibited
124 embryos (Fig. 2) indicating that filopodia were formed. Previously reported
125 exogastrulation was induced by the loss of pseudopodia (Dan and Okazaki, 1956;
126 Hoshi, 1979; Khurrum et al., 2004), therefore, partial exogastrulation in this report was
127 expected to occur by a different mechanism.
128

129 **H^+/K^+ ion pump inhibition perturbed whole embryonic pH and cytoskeletal**

130 **distributions**

131 The intracellular distribution of F-actin and pH was analyzed at the primary

132 invagination stage (steps 1 and 2) to reveal the mechanism underlying the

133 morphological changes in the inhibited embryos at the secondary invagination stage

134 (steps 3 and 4), (Fig. 3A, B). F-actin was visualized by fluorescence of actinin-GFP, and

135 intracellular pH was estimated with pH indicator, whose fluorescent intensity increased

136 as pH decreased. The polarity of intracellular F-actin and pH distribution was evaluated

137 by estimating the fluorescence intensities ratio between the apical and basal sides of

138 cells.

139 Similar apical/basal ratio distributions of actinin-GFP intensities were obtained between

140 the control and inhibited embryos, while the ratios gradually increased closer to the

141 vegetal pole in both embryos at step 1 (Fig. 3C, D, Fig. S1A, B). The distribution of the

142 apical/basal ratios of actinin-GFP intensities in step 2 were similar between control and

143 inhibited embryos only in the animal half (Fig. 3E, Fig. S1C). The ratios of the control

144 embryos from the equator to the vegetal pole was larger than that of inhibited embryos,

145 while nearest the vegetal pole, control embryos showed smaller ratio than that of

146 inhibited embryos. Therefore, the formation of an anomalous embryonic shape of

147 inhibited embryos correlated with the deviation of intracellular F-actin polarity in the

148 vegetal half of the embryos in primary invagination.

149 The apical/basal ratio of the pH indicator was greater than one in both control and

150 inhibited embryos in step 2 (Fig. 3F, Fig. S1D, S2) indicating that the pH on the apical

151 side of each cell was always lower than that on the basal side. Additionally, this ratio
152 was higher in the vegetal half than that in the animal half in the control embryo, while
153 this pattern disappeared in the inhibited embryo (Fig. 3F, Fig. S2). Thus, the polarity of
154 the pH indicator fluorescent intensities was positively correlated with that of actinin-
155 GFP in whole embryos (Fig. 3E, F).

156 Meanwhile, inhibition of the H^+/K^+ ion pump did not influence the whole
157 embryonic distribution of fibropellin-1 (Fig. 3G, H), a F-actin scaffold in the apical
158 lamina of the apical pole (Burke et al., 1998; Nakajima and Burke, 1996).

159

160 **Gastrulation starts but does not progress in embryos with knocked out**
161 **cytoskeleton regulators**

162 CRISPR-Cas9-mediated knockout of the typical enhancer and repressor of F-actin
163 formation (*RhoA* and *YAP1*) (Beane et al., 2006; Dupont et al., 2011) was performed by
164 microinjection of sgRNAs designed with *Cas9* mRNA (Fig. S3) to elucidate the
165 contribution of F-actin to the gastrulation process. Although the mutation frequencies of
166 *RhoA* and *YAP1* knockout were 55.6% and 77.8%, respectively, and the frameshift rate
167 was 22.3% in either knockout (Fig. S3), the gastrulation stopped at step 2 at the primary
168 invagination stage in either *RhoA* or *YAP1* knockout embryos (Fig. 4A) and normal
169 gastrulation and exogastrulation were not observed. Interestingly, the phenotypes
170 between these gene knockout embryos were similar, although the gene functions are
171 different (Fig. S3). Pigmented cells were observed at 45 hpf indicating that development
172 had not ceased. This showed that primary invagination occurred even in embryos with

173 mild perturbation of F-actin function, but subsequent gastrulation processes required
174 appropriate F-actin-derived forces.
175 The whole embryonic distribution of average intensity and apical/basal ratios of the
176 pH indicator was unchanged in *RhoA*-knockout embryos compared with the control, and
177 therefore, perturbation of F-actin polymerization did not affect the pH gradient of the
178 cell (Fig. 4B, C).
179
180 **Mathematical model of embryonic shape formations in early gastrulation**
181 **considering cell-dependent F-actin polarity**
182 A mathematical model of cell motion at the cross section including animal and vegetal
183 poles during steps 1-3 of gastrulation was constructed to examine the influence of
184 intracellular F-actin distribution on the formation of embryonic shapes. The model was
185 constructed based on that of gastrulation in *Nematostella vectensis* (Tamulonis et al.,
186 2011) that consisted of cells constructed by springs and beads circularly connected to
187 form a 2-dimensional cross section of the embryo. The following assumptions were
188 made based on experimentally known facts.
189 I) Each embryo contained three cell types: pigment cells (Takata and Kominami, 2004),
190 wedge cells (Burke at al., 1991), and other cells (Fig. 5). The pigment cells near the
191 entrance to the cavity were assumed to be bottle-shaped (Takata and Kominami, 2004)
192 because of the site-specific force in these cells. This may explain the bending of the
193 vegetal plate occurring in embryos with knocked out F-actin polymerization regulators
194 (Fig. 4), or a surgically removed animal pole (Ettensohn, 1984). The apical length was

195 sufficiently shorter than the basal length and the apical sides of wedge cells were wider
196 than the basal side (Fig. 5A) to form a similar shape to previously observed embryos
197 (Kominami and Takata, 2004).
198 II) The width of the apical and basal sides changes in a cell-dependent manner in
199 control and inhibited embryos due to cytoskeletal forces generated by F-actin. The
200 apical side elongation was expected to correlate with F-actin concentration because
201 higher F-actin concentration was expected to generate stronger cell cortical forces.
202 Thus, the lengths of the apical and basal sides of cells, except pigment cells and wedge
203 cells, were determined based on their apical/basal ratios of actinin-GFP intensities at
204 step 2 (Fig. 5A).
205 III) The cell divisions and 3-dimensional mutual cell invasions mainly contributing to
206 late gastrulation were not included because these processes were rarely observed in
207 early gastrulation (Mizoguchi, 1999). Therefore, the present model described embryo
208 shape dynamics of the control and inhibited embryos as 2-dimensional motions and
209 deformations of the apical and basal sides of 64 cells (Fig. 5A).
210 The simulations showed different shapes (Fig. 5B), although each shape was like
211 that experimentally observed at step 3 (Fig. 1). Similar temporal changes in roundness
212 indices (Fig. 5C) of control embryos (0.85 ~ 0.9) and inhibited embryos (0.75 ~ 0.8)
213 were observed in the simulated data (Fig. 5D, Fig. S4A) and experimental data (Fig. 5E,
214 Fig. S4B).
215 The simulation where the elongation ratio of the apical side of each cell was a little
216 larger than that of control was also performed, with this model named: “over-polarized

217 embryo" (Fig. 5A, B). The whole embryonic shape of this model resulted in a wider and
218 larger roundness index than the control embryos (Fig. S4A). This suggested that the
219 apical/basal ratio polarity of F-actin distribution in each cell was sensitive to the whole
220 embryonic shape.
221
222 **DISCUSSION**
223 Inhibition of the H^+/K^+ ion pump resulted in abnormal embryo shape with partial
224 exogastrulation due to intracellular apical F-actin distribution at the vegetal pole (Fig. 3,
225 5). F-actin concentrations generating cell cortical forces were significantly larger at the
226 apical side of each cell than that of the basal side in the vegetal half of the control
227 embryos, except for cells at the vegetal pole. Therefore, the apical planes of wedge cells
228 and other cells in the vegetal pole side were expected to be significantly wider than the
229 basal planes. Conversely, the apical plane of cells in the vegetal half of the inhibited
230 embryo were not significantly wider compared to the basal sides due to lower apical F-
231 actin levels. The simulation results showed that such expected features in the vegetal
232 half may progress to normal early gastrulation in the control embryos and partial
233 exogastrulation in the inhibited embryos (Fig. 5). Therefore, appropriate embryonic
234 intracellular apical F-actin distribution in the vegetal half is required for gastrulation.
235 One recent study suggested an outer intestinal embryo is formed by Rab35
236 knockdown that might disturb the whole embryonic intracellular F-actin polarity
237 (Remsburg et al., 2021). The results of the present study support this suggestion, and
238 further indicate that the intracellular F-actin polarity on the vegetal pole side of the

239 embryo is particularly important for accurate gastrulation and the intracellular pH
240 controlled by H^+/K^+ ion pump is involved in this process.
241 Gastrulation does not proceed when apical lamina is inhibited (Burke et al., 1991).
242 The whole embryonic distributions of apical lamina along cells were nearly identical
243 between the control and inhibited embryos, although large differences were observed
244 between the cell shapes in the vegetal half and whole embryos. This indicated that the
245 generated force was independent of the relative amounts of apical lamina in each cell.
246 Embryos with partial knockout of F-actin regulating factors (*RhoA* or *YAP1*) stopped the
247 gastrulation at the primary invagination step (Fig. 4A, B). This indicated that the
248 seconday invagination is inhibited without appropriately regulated F-actin, even if the
249 apical lamina exists. Therefore, the apical lamina was suggested to be the scaffold for
250 apical F-actin to generate the force required for the deformation processes driving the
251 secondary invagination of gastrulation and whole embryonic deformation.
252 CRISPR-Cas9-mediated *RhoA* knockout showed intermediate level (55.6%) of
253 mutation frequency (Fig. S3) and the knockout embryos exhibited the primary
254 invagination. However, LV embryos expressing dominant negative RhoA failed to
255 initiate primary invagination (Beane et al., 2006). Therefore, contribution of F-actin
256 function is considerable for the primary invagination, but the extent of the dependency
257 on F-actin function is less and a mechanism other than the F-actin-related system might
258 be involved in this initial process. As mentioned above, F-actin function must be
259 essential for the secondary invagination.
260 The F-actin network formation generating cell cortical forces was drastically

261 enhanced with decreased pH *in vitro* (Köhler et al., 2012) (25). The lower pH at the
262 apical side compared with the basal side was maintained by H^+/K^+ ion pump activity.
263 Whole embryonic distributions of apical/basal ratios of pH indicator at step 2 correlated
264 with those of intracellular actinin-GFP (Fig. 3D, F) suggesting that the F-actin
265 concentration was high when the pH was low at the apical side of cells. Additionally,
266 the apical/basal F-actin polarity in each cell significantly decreased in the vegetal half of
267 the embryo by inhibiting H^+/K^+ ion pump activity (Fig. 3E). Conversely, the whole
268 embryonic distribution of intracellular pH and polarity was unchanged even when F-
269 actin polymerization was directly perturbed by knockout of F-actin regulating factors
270 (Fig. 4D). This suggested that the intracellular pH controlled by the H^+/K^+ ion pump is a
271 one-sided regulator of F-actin polymerization.
272 Inhibition of the H^+/K^+ ion pump did not influence on the whole embryonic
273 distribution of the apical lamina (Fig. 3G, H). This suggested that the regulation of F-
274 actin intracellular distribution by pH is independent of the apical lamina. The embryo
275 exhibited partial exogastrulation if the intracellular pH polarity at the primary
276 invagination stage was weaken by inhibiting H^+/K^+ ion pump activity. This indicated
277 that H^+/K^+ ion pump activity in the primary invagination stage provided a dominant
278 contribution to the progress of the normal secondary invagination to form appropriate
279 intracellular F-actin polarity in the whole embryo.
280 The influence of pH on F-actin network formation and force generation is a
281 universal biochemical feature confirmed by *in vitro* experiments (Köhler et al., 2012).
282 Inhibition of H^+/K^+ ion pump activity significantly decreases intracellular pH in the LV

283 embryo (Schatzberg et al., 2015), while an increase in the intracellular pH was observed
284 in the majority of cells in the HP embryo (Fig. S5). Decreases in the intracellular pH of
285 LV may induce increases in the apical/basal polarities of intracellular pH and F-actin
286 concentration like the "over-polarized embryo" model. The over-polarized embryo
287 model exhibited a wider embryonic shape with a larger roundness index than the control
288 embryos (Fig. 5B, S4B) which is consistent with LV imaging (Schatzberg et al., 2015).
289 This supported the suggestion that H^+/K^+ ion pump activity significantly contributed to
290 early gastrulation through the regulation of intracellular F-actin apical/basal
291 polarizations.

292 Omeprazole treatment of sea urchin embryos disrupts the left-right asymmetric
293 formations of the adult rudiment although gastrulation is completed (Bessodes et al.,
294 2012; Duboc et al., 2005; Hibino et al., 2006). The left-right asymmetric *nodal* gene
295 expression observed immediately after gastrulation is important for establishing this
296 asymmetry (Duboc et al., 2005). Frogs, chickens, zebrafish, and ascidians disrupt left-
297 right asymmetry by inhibiting H^+/K^+ ion pump activity (Kawakami et al., 2005; Levin
298 et al., 2002; Shimeld and Levin, 2006). Disrupted left-right asymmetry in HP is
299 observed at lower (~ 3/5 times) omeprazole concentrations (Hibino et al., 2006) than
300 those in this study. Inhibition of H^+/K^+ pump activity by dilute omeprazole solutions
301 induced weak perturbation of gut formation in this study, which may disrupt cell-cell
302 interactions and regulate whole embryonic *nodal* gene expression.

303 This report revealed the close relationship between pH, F-actin, and H^+/K^+ ion
304 pump activity inducing normal/abnormal gastrulation in sea urchins through

305 intracellular F-actin regulation. Embryonic F-actin distribution on the apical side of
306 each cell was important for normal gastrulation, and H^+/K^+ ion pump activity may be
307 involved in F-actin distribution. This finding provides key insights into the evolutionary
308 relationship between development and morphogenesis. Intracellular apical/basal
309 polarity of pH showed different cellular features between vegetal and animal poles in
310 step 2 of gastrulation. However, the formation of these position-dependent intracellular
311 states was not explored. Therefore, upstream regulators of H^+/K^+ ion pump activity
312 should be investigated to reveal the detailed morphogenesis molecular mechanism. The
313 universal effect of inhibiting H^+/K^+ ion pump activity on early embryo formation among
314 different animals will be tested in the future.
315

316 **MATERIALS AND METHODS**

317 **Animals and embryos**

318 Adult Japanese sea urchins (HP) were collected from Seto Inland Sea or Tateyama Bay.
319 Eggs and sperm were obtained by coelomic injection of 0.55 M KCl. Fertilized eggs
320 were cultured in filtered seawater at 16°C.
321

322 **Inhibition of H^+/K^+ ion pump by omeprazole**

323 A 100 mM stock solution of omeprazole (FUJIFILM Wako Pure Chemical Corporation,
324 Japan) dissolved in dimethyl sulfoxide (DMSO) was immediately added to fertilized
325 eggs to a final concentration of 100 μM and cultured at 16°C.
326

327 ***In situ* nucleus and F-actin visualization in embryos**

328 Sea urchin embryos were fixed by immersion in fixative III (4% paraformaldehyde,
329 32.5% filtered seawater, 32.5 mM 3-(N-morpholino)propane sulfonic acid (MOPS), pH
330 7.0, 162.5 mM NaCl) for 16 h at 4°C. Embryos were washed three times using 0.5 mL 1
331 x phosphate buffered saline (PBS), stored in 100% ethanol at -20°C, and used within 1
332 week. Fixed embryos were washed three times with 1 x PBS, permeabilized with 0.5%
333 Triton X-100 for 20 min at room temperature, washed three times with 1 x PBS, and
334 stained with 100 nM phalloidin (in 1 x PBS) for 45 min at room temperature. Stained
335 embryos were washed three times with 1 x PBS, mounted in SlowFade Gold antifade
336 mountant with DAPI (Molecular Probes) and observed using a confocal laser scanning
337 microscopy (Carl Zeiss LSM 700, Germany) with laser illumination at 405/435 nm
338 excitation/emission for DAPI and 555/573 nm excitation/emission for phalloidin,
339 respectively.

340

341 **Live imaging of pH, actinin, and apical lamina**

342 Intracellular pH of sea urchin embryos was visualized using pHrodo Red AM
343 intracellular pH indicator or 5-(and-6)-carboxy SNARF-1 (C-1270) (ThermoFisher
344 Scientific, USA) at final concentrations of 10 μM and 5 μM, respectively, and stained at
345 16°C for 30 min. The embryos were washed in filtered seawater and observed using
346 confocal microscopy with laser illumination at 555/585 nm excitation/emission for
347 pHrodo and 555/573 m excitation/emission for SNARF-1, respectively.

348 Actinin and fibropellin-1 were visualized following fusion of the proteins with GFP.
349 RNA was extracted from mesenchyme blastula stage HP embryos using ISOGEN
350 (Nippongene, Japan) according to the manufacturer's instructions. Actinin and
351 fibropellin-1 coding sequences were amplified by RT-PCR using SuperScript™ III
352 Reverse Transcriptase (Thermo Fisher Scientific, USA) with the primers stated in Table
353 S1 and cloned into pGreenLantern2-derived plasmid at restriction sites EcoRI and
354 XhoI. mRNA (actinin-GFP, fibropellin-1-GFP, in that order) was synthesized *in vitro*
355 using an mMESSAGE mMACHINE T7 ultra transcription kit (ThermoFisher Scientific,
356 USA) and purified using an RNeasy mini kit (Qiagen, Nederland). mRNA was
357 microinjected into fertilized eggs as described by Liu et al., (2019).
358 Fluorescent images were acquired by confocal microscopy using an excitation of
359 488 nm, and emission of 515 nm. The images of the animal and vegetal poles of the
360 embryo were analyzed based on the *z*-stack image with the largest area by averaging
361 seven *z*-axis images with a total thickness of 6 μm.
362
363 **Quantification of experimental images**
364 The fluorescent images of embryos were acquired according to the angle θ (0°~180°)
365 between the vegetal and animal poles along the circumference (Fig. S6) and
366 transformed into a band-like image using the "Polar Transformer" function
367 (https://imagej.nih.gov/ij/plugins/polar-transformer.html) of ImageJ 2.1.0. Each band-
368 like image was filtered using a median filter (radius = 1.0). The filtered images were
369 binarized using "Mean" (pHrodo indicator), "IsoData" (actinin), and "Triangle"

370 (fibropellin-1 and SNARF-1) functions, respectively, to obtain the cellular regions of
371 the embryo. The apical/basal ratios of the pH indicator, actin-GFP, and fibropellin-1-
372 GFP for θ were determined using average fluorescent intensities over the regions with
373 the width of 3.126 μm from the apical and basal sides.

374 The fluorescent intensity of the pHrodo indicator was defined by the average
375 fluorescent intensity over the intracellular region with a width of 6.232 μm from the
376 apical side (Fig. S6). Fluorescent values were estimated by taking the ratio between the
377 observed fluorescence intensity and the average background fluorescence intensity
378 around the entire embryo.

379 F-actin and apical lamina were stained by mRNA microinjections of actinin-GFP
380 and fibropellin-1-GFP to fertilized eggs. Nonnegligible variations was inevitable in the
381 concentration of injected mRNA among fertilized egg samples, which would be
382 amplified during development. Therefore, only the apical/basal ratios were used to
383 evaluate the intracellular features of F-actin and apical lamina distributions.

384 Two data points were obtained for each θ from each fluorescence image of the
385 embryo since the left and right sides of the embryo were considered axis symmetric
386 against the animal-vegetal axis. Both data were used to estimate the sample average and
387 95% confidence interval of each value, where the number of samples (n) was given by 2
388 × [number of observed embryos].

389

390 **Gene knockout by CRISPR-Cas9**

391 Knock out of endogenous *RhoA* and *YAP1* in HP was performed using the method

392 described by Liu et al., (2019). The oligonucleotide sequences used in sgRNA
393 preparations were listed in Table S2.
394
395 **Heteroduplex mobility assay (HMA) and DNA sequencing analysis**
396 Analysis of knockout embryos by HMA and DNA sequencing was performed according
397 to Liu et al., (2019). The primer sequences used to amplify each target region were
398 listed in Table S3.
399
400 **Mathematical model of sea urchin embryos**
401 A 2-dimensional particles model describing cellular motion at the cross section of
402 animal poles and vegetal poles of sea urchin embryos during steps 1 to 3 of gastrulation
403 was constructed. The determined number of cells was based on that at the equatorial
404 plane of the embryo at the blastula stage (Mizoguchi, 1999). The following assumptions
405 were made: 1) each cell was represented by 16 particles with radii (r) of 1.125 μm, and
406 each embryo was represented by 64 cells connected in a ring (Fig. S7). 2) Each cell
407 perimeter was 36 μm and the height and width of the embryo at step 1 was 110 μm and
408 100 μm, respectively, which was consistent with sea urchin embryo observations
409 (results not shown). 3) The number of cells was constant because cell divisions and
410 cell invasions from other cross-sections were rarely observed during the primary
411 invagination stage (Mizoguchi, 1999). 4) The motion of each particle obeyed the
412 following overdamped limit of the equation of motion:

$$\frac{\partial \boldsymbol{X}_{i,j}}{\partial t} = -\frac{1}{\gamma}\frac{\partial V}{\partial \boldsymbol{X}_{i,j}} \qquad (1),$$

where $\boldsymbol{X}_{i,j} = (x_{i,j}(t), y_{i,j}(t))$ is the position of the *j*-th particle constructing the *i*-th cell (*i* = 0,1,2…63 and *j* = 0,1,2…15) on the x–y plane at time *t* (Fig. 5, Fig. S7), *γ* is the coefficient of the drag force acting on each particle, and V is the potential of the entire system. 5) The y-axis was parallel to the animal-vegetal axis of the embryo model. We rewrote $\frac{V}{\gamma} = U$ and U was calculated by:

$$U = U_{bond} + U_{collision} + U_{actin} + U_{adhesion} + U_{ca} + U_{ea} \qquad (2),$$

where U_{bond} is the elastic force potential between each neighboring pair of particles in each cell to maintain each cell perimeter, denoted by:

$$U_{bond} = \sum_{i=0}^{63}\sum_{j=0}^{15}\frac{k_b}{2}(d_{(i,j),(i,j+1)} - 2r)^2 \qquad (3),$$

where k_b, $d_{(i,j),(i,j+1)}$, and *r* are the coefficient of elasticity, the distance between the *j*-th and *j* +1-th particle ($j + 1 = 0$ for $j = 15$) in the *i*-th cell at time *t*, and the particle radius, respectively.

$U_{collision}$ is the potential of excluded volume effects among all particles denoted as follows:

$$U_{collision} = \sum_{i<k}\sum_{j<l}\theta(2r - d_{(i,j),(k,l)})\frac{k_c}{2}(2r - d_{(i,j),(k,l)})^2 \qquad (4),$$

where k_c is the coefficient of repulsion between two particles, and $\theta(x)$ is the Heaviside step function.

U_{actin} is the elastic force potential to form and sustain cell shape with the expansion and contraction of the apical and basal sides by the cytoskeleton denoted as follows:

$$U_{actin} = \sum_i \frac{k_a}{2}((d_{(i,10),(i,14)} - l_i^a)^2 + (d_{(i,2),(i,6)} - l_i^b)^2) \qquad (5),$$

where the apical and basal sides of the *i*-th cell consisted of particles with *j* = 10 –14 and *j* = 2 – 6, respectively. The wideness of the apical and basal sides at time *t* were given by $d_{(i,10),(i,14)}$ and $d_{(i,2),(i,6)}$, respectively. The basic wideness of the apical and basal sides were given by l_i^a and l_i^b, respectively. k_a was assumed by the coefficient of elasticity to sustain the wideness of the apical and basal sides of the cell.

$U_{adhesion}$ is the potential force for cell adhesion by proteins such as cadherin, and is denoted as follows:

$$U_{adhesion} = \sum_i \sum_j \frac{k_h}{2}(d_{(i,j),(i+1,k(j))} - 2r)^2 \qquad (6),$$

where k_h is the coefficient for the adhesive forces between the particles of the *i*-th and *i* + 1-th cells ($i + 1 = 0$ for $i = 63$), and $k(j) \equiv 6, 7, 8, 9, 10$ for $j \equiv 2, 1, 0, 15, 14$, respectively (Fig. S7).

U_{ca} is the potential of the forces to conserve each cell area denoted as follows:

$$U_{ca} = \sum_i \frac{k_{ca}}{2}(s_i - s_i^{ini})^2 \qquad (7),$$

where k_{ca} is the coefficient of elasticity required to maintain each cell area. The area of the *i*-th cell was estimated by $s_i = \sum_{j=0}^{15} \left| \boldsymbol{X_{i,j}} - \boldsymbol{X_i^{cc}} \right|$ with $\boldsymbol{X_i^{cc}} = \frac{1}{16}\sum_{j=0}^{15} \boldsymbol{X_{i,j}}$, and s_i^{ini} referred to s_i given by $\boldsymbol{X_{i,j}}$ at the initial state.

U_{ea} is the potential of the forces to maintain the area (volume) of the sea urchin embryo and denoted as follows:

$$U_{ea} = \frac{k_{ea}}{2}(S - S^{ini})^2 \qquad (8),$$

where k_{ea} is the coefficient of elasticity required to maintain embryo area. The area was estimated by $S = \sum_{i=0}^{63} |\boldsymbol{X_i^{cc}} - \boldsymbol{X^{ec}}|$ with $\boldsymbol{X^{ec}} = \frac{1}{64}\sum_{i=0}^{63} \boldsymbol{X_i^{cc}}$, and S^{ini} referred to S given by $\boldsymbol{X_{i,j}}$ at the initial state.

U_{ca} and U_{ea} were considered the alternatives of the volume-conserving forces in real 3-D cells and embryos as internal pressures in each cell and embryo are considered isotropic.

Simulation method of mathematical model

The simulations of the present mathematical model were performed through the integrals of equation of motion (1) using Euler method with time intervals of 0.000064 h with conserved $\boldsymbol{X^{ec}} = (0, 0)$. In all models, the parameters k_{bond}, $k_{collision}$, k_{actin}, $k_{adhesion}$, k_{ca}, and k_{ea} were given empirically as 9375, 6250, 8125, 8125, 625, and 0.00625 hour^{-1}, respectively, because there were no experiments to measure or estimate them. The qualitative features of the results were independent of the details of these values if the order was maintained. The model formed the embryo shape at step 1 of gastrulation if the appropriate cell type-dependent values of l_i^a and l_i^b, $= l_i^{a,ini}$ and $l_i^{b,ini}$ were given for the models of pigment cells, wedge cells, and other cells (Fig. 5). This configuration gave the particle positions $\boldsymbol{X_{i,j}}$ at time t = 0 (initial configuration) in all simulations.

The early gastrulation processes were simulated by the change in l_i^a and l_i^b respectively, from $= l_i^{a,ini}$ and $l_i^{b,ini}$ to $= l_i^{a,fin}$ and $l_i^{b,fin}$ at time $t = 0$. Here, $l_i^{a,fin}$

and $l_i^{b,fin}$ were assumed to obey $l_i^{a,fin} + l_i^{b,fin} = l_i^{a,ini} + l_i^{b,ini} =$ constant among cells except pigment cells based on the expectation that F-actin was constant. The model showed similar structural behaviors to the early gastrulation as the relaxation process of $d_{(i,10),(i,14)} \rightarrow l_i^{a,fin}$ and $d_{(i,2),(i,6)} \rightarrow l_i^{b,fin}$.

Statistical analysis

All experiments were performed independently 2 times or more with 4 replicates or more per experiment. Statistical test was performed using SciPy library (https://www.scipy.org/). The roundness index of the vegetal side of each embryo was evaluated by: [embryo width half-way between the bottom and middle of the embryo]/[embryo length] (Fig. 5C).

Acknowledgements

We thank Prof. Masato Kiyomoto (Tateyama Marine Laboratory, Ochanomizu University) for supplying live sea urchins. We would like to thank Editage (www.editage.com) for English language editing.

Competing interests

No competing interests declared.

Author Contributions

K.W., N.S., and A.A. conceived and designed the study; K.W., Y.K., and N.S. conducted the experiments; K.W., Y.Y., M.F., and A.A. analyzed the data; K.W. and A.A. conducted the mathematical model construction and simulations; K.W., N.S., and A.A. wrote the manuscript with support from all authors; T.Y. supervised the work.

Funding information

This work was supported by JSPS KAKENHI [grant, award number: 17K05614, 21K06124 to A.A.]; and JSPS KAKENHI [grant, award number: 17K07241, 20K06602 to N.S.]; JSPS KAKENHI [grant, award number: 19K20382 to M.F]; SASAGAWA SCIENTIFIC RESERCH GRANT, [award number: 2021-4023, to K.W.]; Hiroshima University Graduate School Research Fellowship, 2021-2024 (InformationAI Field, to K.W.);.

References

Aihara M. and Amemiya, S. (2001). Left-right positioning of the adult rudiment in sea urchin larvae is directed by the right side. *Development* **128**(24), 4935-4948. doi:10.1242/dev.128.24.4935

Beane, W. S., Gross, J. M. and McClay, D. R. (2006). RhoA regulates initiation of invagination, but not convergent extension, during sea urchin gastrulation. *Dev. Biol*. **292**(1), 213-225. doi:10.1016/j.ydbio.2005.12.031

Bessodes, N., Haillot, E., Duboc, V., Röttinger, E., Lahaye, F. and Lepage, T.

518 (2012). Reciprocal signaling between the ectoderm and a mesendodermal left-
519 right organizer directs left-right determination in the sea urchin embryo. *PLoS*
520 *Genet*. **8**(12), e1003121. doi:10.1371/journal.pgen.1003121
521 **Burke, R. D., Lail, M. and Nakajima, Y.** (1998). The apical lamina and its role in cell
522 adhesion in sea urchin embryos. *Cell Adhesion Comm*. **5**(2), 97-108.
523 doi:10.3109/15419069809040284
524 **Burke, R. D., Moller, D. J., Krupke, O. A. and Taylor, V. J.** (2014). Sea urchin
525 neural development and the metazoan paradigm of neurogenesis. *Genesis* **52**(3),
526 208-221. doi:10.1002/dvg.22750
527 **Burke, R. D., Myers, R. L., Sexton, T. L. and Jackson, C.** (1991). Cell movements
528 during the initial phase of gastrulation in the sea urchin embryo. *Dev. Biol*.
529 **146**(2), 542-557. doi:10.1016/0012-1606(91)90255-2
530 **Dan, K. and Okazaki, K.** (1956). Cytoembryological studies of sea urchins: III. Role
531 of the secondary mesenchyme cells in the formation of the primitive gut in sea
532 urchin larvae. *Biol. Bull.* **110**, 29-42.
533 **Davidson, E. H., Rast, J. P., Oliveri, P., Ransick, A., Calestani, C., Yuh, C. H.,**
534 **Minokawa, T., Amore, G., Hinman, V., Arenas-Mena, C., Otim, O., Brown,**
535 **C. T., Livi, C. B., Lee, P. Y., Revilla, R., Schilstra, M. J., Clarke, P. J., Rust,**
536 **A. G., Pan, Z., Arnone, M. I., Rowen, L., Cameron, R. A., McClay, D. R.,**
537 **Hood, L. and Bolouri, H.** (2002). A provisional regulatory gene network for
538 specification of endomesoderm in the sea urchin embryo. *Dev. Biol.*, **246**(1), 162-
539 190. doi: 10.1006/dbio.2002.0635

Davidson, L. A., Koehl, M. A., Keller, R. and Oster, G. F. (1995). How do sea urchins invaginate? Using biomechanics to distinguish between mechanisms of primary invagination. *Development* **121**(7), 2005-2018. doi:10.1242/dev.121.7.2005

Duboc, V., Röttinger, E., Lapraz, F., Besnardeau, L. and Lepage, T. (2005). Left-right asymmetry in the sea urchin embryo is regulated by nodal signaling on the right side. *Dev. Cell*. **9**(1), 147-158. doi:10.1016/j.devcel.2005.05.008

Dupont, S., Morsut, L., Aragona, M., Enzo, E., Giulitti, S., Cordenonsi, M., Zanconato, F., Le Digabel, J., Forcato, M., Bicciato, S. et al. (2011). Role of YAP/TAZ in mechanotransduction. *Nature* **474**(7350), 179-183. doi:10.1038/nature10137

Ettensohn, C. A. (1984). Primary invagination of the vegetal plate during sea urchin gastrulation. *Amer. Zool.* **24**(3), 571-588. doi:10.1093/icb/24.3.571

Gustafson, T. and Kinnander, H. (1956). Microaquaria for time-lapse cinematographic studies of morphogenesis in swimming larvae and observations on sea urchin gastrulation. *Exp. Cell Res*. **11**(1), 36-51. doi:10.1016/0014-4827(56)90188-4

Gustafson, T. and Kinnander, H. (1960). Cellular mechanisms in morphogenesis of the sea urchin gastrula: The oral contact. *Exp. Cell Res.* **21**(2), 361-373. doi:10.1016/0014-4827(60)90268-8

Hardin, J. D. and Cheng, L. Y. (1986). The mechanisms and mechanics of archenteron elongation during sea urchin gastrulation. *Dev. Biol*. **115**(2), 490-

562 501. doi:10.1016/0012-1606(86)90269-1

563 **Hibino, T., Ishii, Y., Levin, M. and Nishino, A.** (2006). Ion flow regulates left-right
564 asymmetry in sea urchin development. *Dev. Genes Evol*. **216**(5), 265-276.
565 doi:10.1007/s00427-005-0051-6

566 **Hoshi, M.** (1979). Exogastrulation induced by heavy water in sea urchin larvae. *Cell*
567 *Differ*. 8(6), 431-5. doi:10.1016/0045-6039(79)90039-3

568 **Kawakami, Y., Raya, Á., Raya, R. M., Rodríguez-Esteban, C. and Izpisúa**
569 **Belmonte, J. C.** (2005). Retinoic acid signalling links left-right asymmetric
570 patterning and bilaterally symmetric somitogenesis in the zebrafish embryo.
571 *Nature* **435**(7039), 165-171. doi:10.1038/nature03512

572 **Khurrum, M., Hernandez, A., Eskalaei, M., Badali, O., Coyle-Thompson, C. and**
573 **Oppenheimer, S. B.** (2004). Carbohydrate involvement in cellular interactions in
574 sea urchin gastrulation. *Acta Histochem*. **106**(2), 97-106. doi:
575 10.1016/j.acthis.2004.01.001

576 **Kimberly, E. L. and Hardin, J.** (1998). Bottle cells are required for the initiation of
577 primary invagination in the sea urchin embryo. *Dev. Biol*. **204**(1), 235-50.
578 doi:10.1006/dbio.1998.9075

579 **Köhler, S., Schmoller, K. M., Crevenna, A. H., Bausch, A. R.** (2012). Regulating
580 contractility of the actomyosin cytoskeleton by pH. *Cell Rep*. **2**(3), 433-439.
581 doi:10.1016/j.celrep.2012.08.014

582 **Kominami, T. and Takata, H.** (2004). Gastrulation in the sea urchin embryo: A model
583 system for analyzing the morphogenesis of a monolayered epithelium. *Dev.*

584 *Growth Differ.* **46**(4), 309-326. doi:10.1111/j.1440-169x.2004.00755.x

585 **Levin, M., Thorlin, T., Robinson, K. R., Nogi, T. and Mercola, M**. (2002).
586 Asymmetries in H^+/K^+-ATPase and cell membrane potentials comprise a very
587 early step in left-right patterning. *Cell* **111**(1), 77-89. doi:10.1016/S0092-
588 8674(02)00939-X

589 **Liu, D., Awazu, A., Sakuma, T., Yamamoto, T. and Sakamoto, N.** (2019).
590 Establishment of knockout adult sea urchins by using a CRISPR-Cas9 system.
591 *Dev. Growth Differ*. **61**(6), 378-388. doi:10.1111/dgd.12624

592 **Martik, M. L. and McClay, D. R.** (2017). New insights from a high-resolution look at
593 gastrulation in the sea urchin, *Lytechinus variegatus*. *Mech. Dev.* **148**, 3-10.
594 doi:10.1016/j.mod.2017.06.005

595 **McCain, E.R. and McClay, D.R.** (1994). The establishment of bilateral asymmetry in
596 sea urchin embryos. *Development* **120**(2), 395-404. doi:10.1242/dev.120.2.395

597 **McClay, D. R., Miranda, E. and Feinberg, S. L.** (2018). Neurogenesis in the sea
598 urchin embryo is initiated uniquely in three domains. *Development* **145**(21),
599 dev167742. doi: 10.1242/dev.167742

600 **Mizoguchi, H.** (1999). Cell numbers in the gut of the embryo of the sea urchin
601 *Hemicentrotus pulcherrimus*. *Zool. Sci*. **16**(2), 341-344. doi:10.2108/zsj.16.341

602 **Nakajima, Y. and Burke, R. D.** (1996). The initial phase of gastrulation in sea urchins
603 is accompanied by the formation of bottle cells. *Dev. Biol.* **179**(2), 436-446.
604 doi:10.1006/dbio.1996.0273

605 **Odell, G. M., Oster, G., Alberch, P. and Burnside, B.** (1981). The mechanical basis

606 of morphogenesis. I. Epithelial folding and invagination. *Dev. Biol*. **85**(2), 46-62.
607 doi:10.1016/0012-1606(81)90276-1
608 **Oliveri, P. and Davidson, E. H.** (2004). Gene regulatory network controlling
609 embryonic specification in the sea urchin. *Curr. Opin. Genet. Dev*., **14**(4), 351–
610 360. doi: 10.1016/j.gde.2004.06.004
611 **Remsburg, C., Testa, M., Song, J. L.** (2021). Rab35 regulates skeletogenesis and
612 gastrulation by facilitating actin remodeling and vesicular trafficking. *Cells &*
613 *Dev.*, **165**(3), 203660. doi: 10.1016/j.cdev.2021.203660
614 **Schatzberg, D., Lawton, M., Hadyniak, S. E., Ross, E. J., Carney, T., Beane, W. S.,**
615 **Levin, M. and Bradham, C. A.** (2015). H^+/K^+ ATPase activity is required for
616 biomineralization in sea urchin embryos. *Dev. Biol.* **406**(2), 259-270.
617 doi:10.1016/j.ydbio.2015.08.014
618 **Serrano Nájera, G. and Weijer, C. J.** (2020). Cellular processes driving gastrulation
619 in the avian embryo. *Mech. Dev*. **163**, 103624. doi:10.1016/j.mod.2020.103624
620 **Shimeld, S. M. and Levin, M.** (2006). Evidence for the regulation of left-right
621 asymmetry in *Ciona intestinalis* by ion flux. *Dev. Dyn*. **235**(6), 1543-1553.
622 doi:10.1002/dvdy.20792
623 **Shindo, A.** (2018). Models of convergent extension during morphogenesis. (2018).
624 *WIREs Dev. Biol*. **7**(1), e293. doi:10.1002/wdev.293
625 **Stower, M. J. and Bertocchini, F.** (2017). The evolution of amniote gastrulation: the
626 blastopore-primitive streak transition. *Wiley Interdiscip. Rev. Dev. Biol*. **6**(2),
627 e262. doi: 10.1002/wdev.262

628 **Takata, H. and Kominami, T.** (2004). Pigment cells trigger the onset of gastrulation in
629 tropical sea urchin *Echinometra mathaei*. *Dev. Growth Differ*. **46**(1), 23-35.
630 doi:10.1111/j.1440-169X.2004.00726.x
631 **Takemoto, A., Miyamoto, T., Simono, F., Kurogi, N., Shirae-Kurabayashi, M.,**
632 **Awazu, A., Suzuki, K.-i. T. and Sakamoto, N.** (2016). Cilia play a role in
633 breaking left-right symmetry of the sea urchin embryo. *Genes Cells* **21**(6), 568-
634 578. doi:10.1111/gtc.12362
635 **Tamulonis, C., Postma, M., Marlow, H. Q., Magie, C. R., de Jong, J. and**
636 **Kaandorp, J.** (2011). A cell-based model of *Nematostella vectensis* gastrulation
637 including bottle cell formation, invagination and zippering. *Dev. Biol.* **351**(1),
638 217-228. doi:10.1016/j.ydbio.2010.10.017
639 **Voiculescu, O., Bodenstein, L., Lau, I. J. and Stern, C. D.** (2014). Local cell
640 interactions and self-amplifying individual cell ingression drive amniote
641 gastrulation. *eLife* **3**, e01817. doi: 10.7554/eLife.01817
642 **Warner, J. F. and McClay, D. R.** (2014). Left-right asymmetry in the sea urchin.
643 *Genesis* **52**(6), 481-487. doi:10.1002/dvg.22752
644 **Yaguchi, S., Yaguchi, J., Angerer, R. C., Angerer, L. M. and Burke, R. D.** (2010).
645 TGFβ signaling positions the ciliary band and patterns neurons in the sea urchin
646 embryo. *Dev. Biol.* **347**(1), 71-81. doi:10.1016/j.ydbio.2010.08.009
647
648
649

650

651

652

653

654

655 **Figures**

656

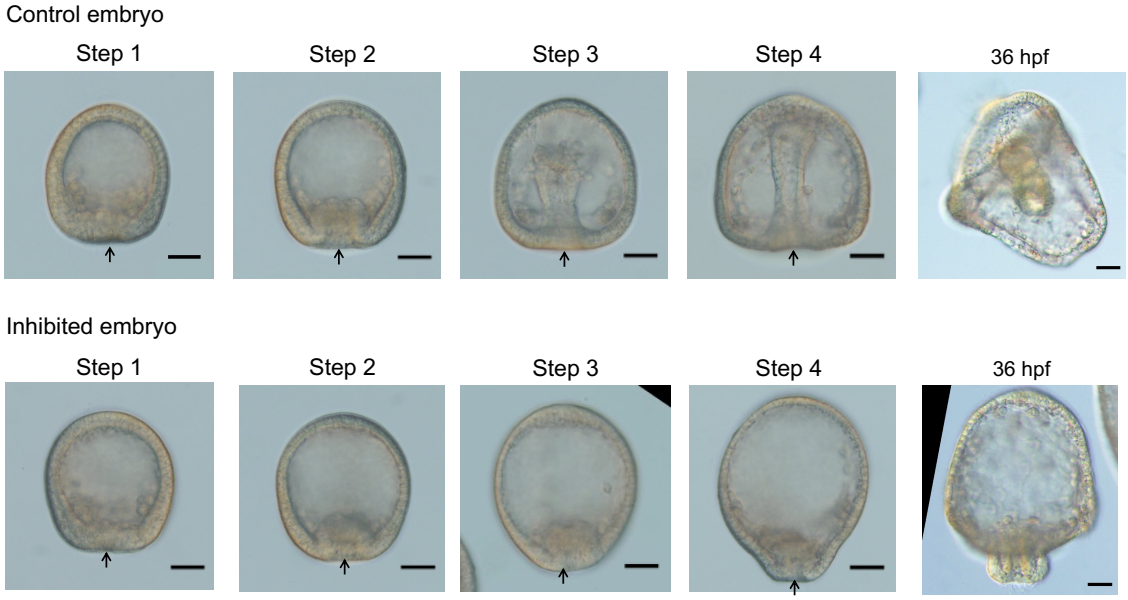

657

658 **Fig. 1. Developmental stages of control and H^+/K^+ ion pump-inhibited HP**

659 **embryos.** Typical bright-field images of the gastrulation process (steps 1-4) and 36 hpf

660 embryos (scale bars: 30 µm). Arrows indicate vegetal pole positions. Gastrulation did

661 not progress after step 2 in the inhibited embryos, and the outward protrusion of the

662 vegetal pole side was more pronounced at step 4. At 36 hpf, "partial" exogastrulation

663 was observed in the inhibited embryo.

664

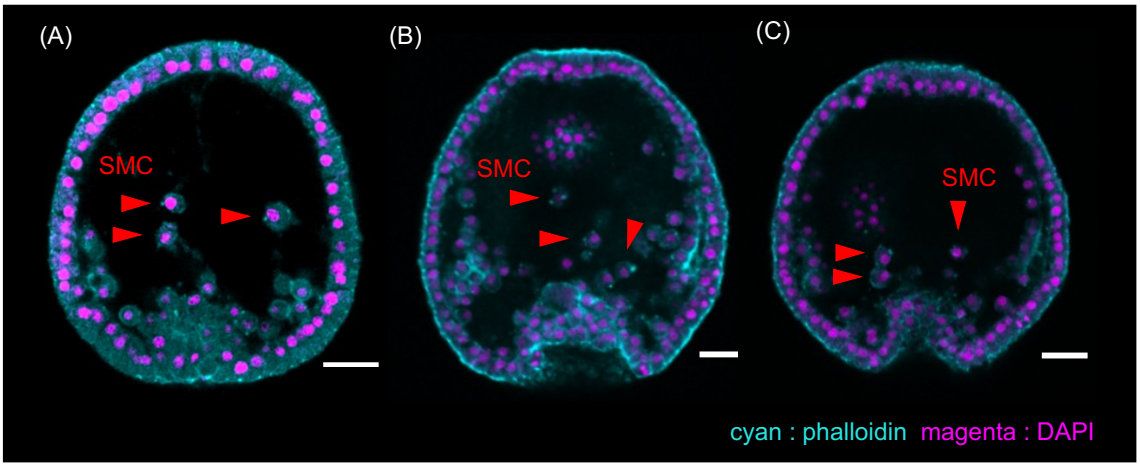

Fig. 2. *In situ* SMC visualization of HP embryo development with inhibited H^+/K^+ ion pumps. Confocal microscopy images at 24 hpf (A), 27 hpf (B), and 29 hpf (C) (scale bars: 25 μm). The nucleus and F-actin in the embryos were stained with DAPI (magenta) and phalloidin (cyan), respectively. SMC migration was confirmed at all developmental stages as indicated by red triangles.

682

683

684

685

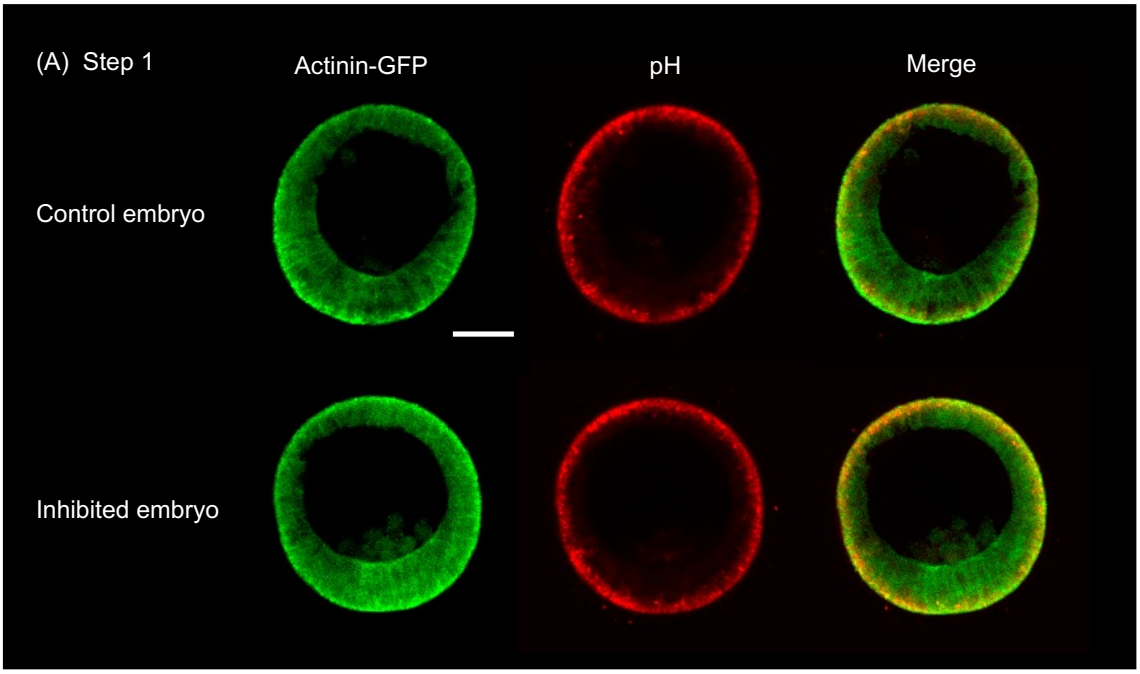

686

687

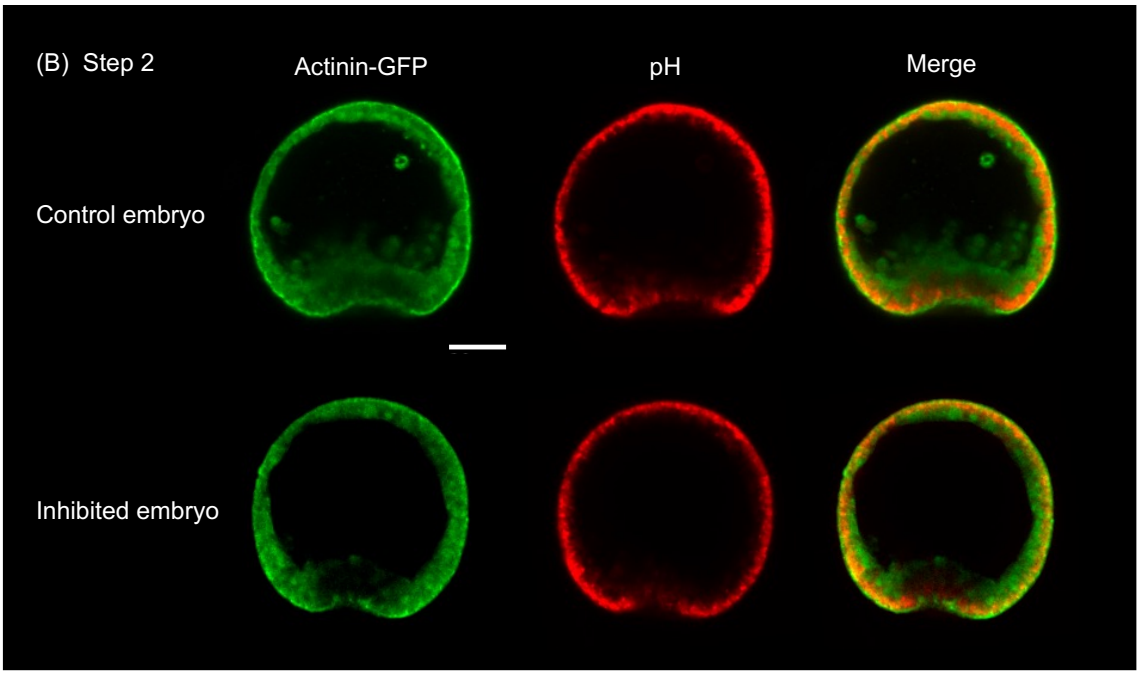
(B) Step 2
Actinin-GFP
pH
Merge
Control embryo
Inhibited embryo

688

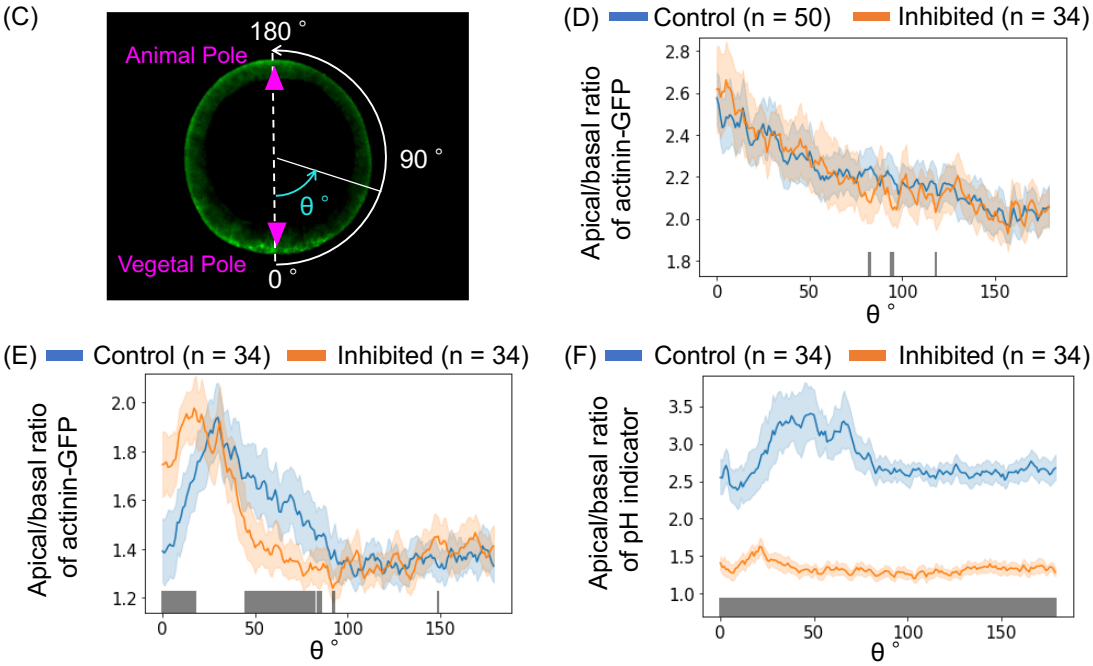
(C)
180 °
Animal Pole
90 °
θ °
Vegetal Pole
0 °
(D) Control (n = 50) Inhibited (n = 34)
Apical/basal ratio of actinin-GFP
θ °
(E) Control (n = 34) Inhibited (n = 34)
Apical/basal ratio of actinin-GFP
θ °
(F) Control (n = 34) Inhibited (n = 34)
Apical/basal ratio of pH indicator
θ °

689

690

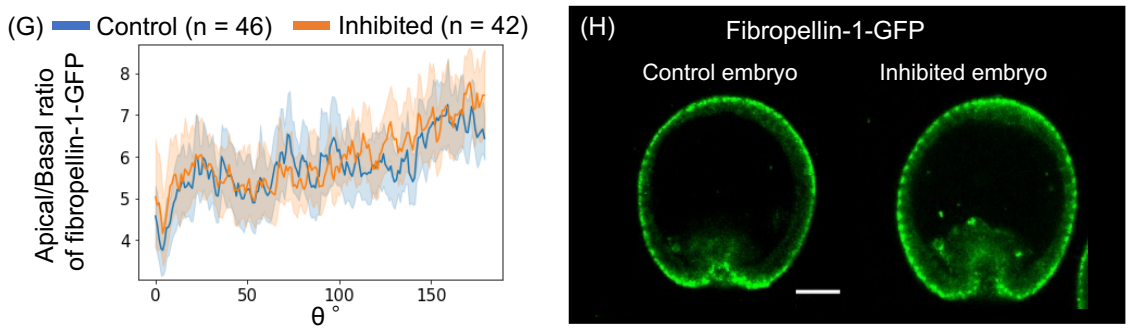

Fig. 3. Whole embryonic distributions of pH, actinin-GFP, and fibropellin-1-GFP. (A-B) Confocal fluorescence microscopy images of co-stained intracellular pH (pH indicator: red) and actinin (actinin-GFP: green) at gastrulation step 1 (A) and step 2 (B) on the cross-section of animal poles and vegetal poles of control and inhibited embryos (scale bars: 30 μm). (C) Definition of angle θ (0°~180°) from the vegetal pole (0°) to the animal pole (180°) along the circumference of the embryo cross-section. (D-F) Average apical/basal ratios and 95% confidence intervals (error bars) at angle θ of actinin-GFP intensities at step 1 (D) and step 2 (E), pH indicator intensities at step 2 (F), and fibropellin-1-GFP intensities at step 2 (G). Blue and orange curves and bars represent the control and inhibited embryo values, respectively. Gray bars indicate significantly different average values between the control and inhibited embryos according to Welch's t-test ($p < 0.05$) (see also Fig. S1.). The correlation coefficients of apical/basal ratios between actinin-GFP intensities (E) and pH indicator intensities (F) in control and inhibited embryos were 0.56 and 0.64, respectively. (H) Fluorescence images of fibropellin-1-GFP from control and inhibited embryos at gastrulation step 2 (scale bars: 30 μm).

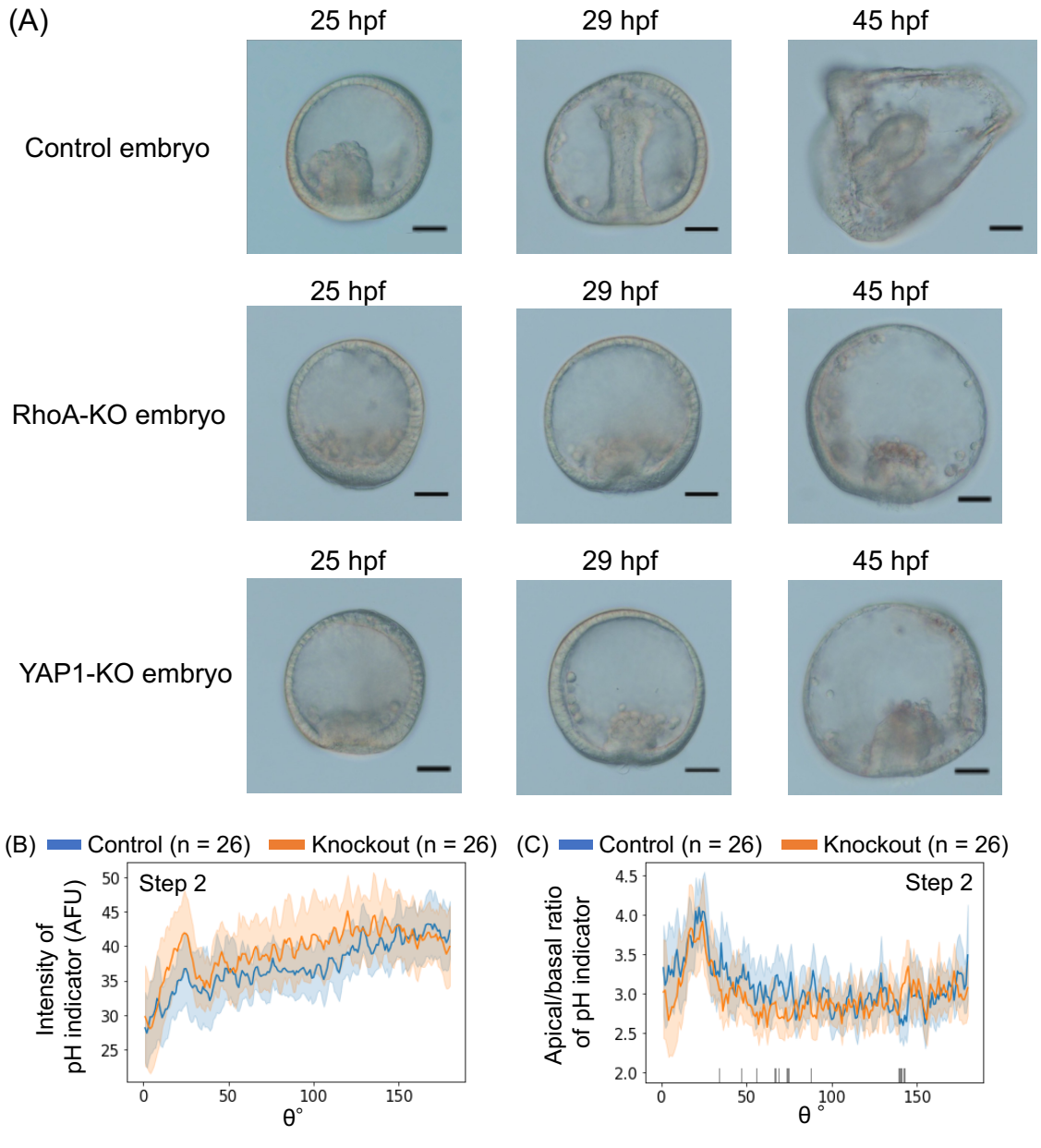

Fig. 4. Effect of F-actin regulator knockout on gastrulation.

(A) Bright-field images of gastrulation (steps 2-3) in control, *RhoA* knockout, and *YAP1* knockout embryos at selected time-points. PMCs and pigment cells were observed in all embryos suggesting that development did not stop. The knockout embryos did not form the structure like prism larva observed at 45 hpf (step 3) in the control embryo (scale bars: 30 μm). (B-C) Average fluorescence intensities (arbitrary fluorescence units) and

95% confidence intervals (error bars) of intracellular pH indicator (B) and apical/basal ratio of pH indicator (C) of *RhoA* knockout embryos and control embryos as a function of angle θ. The meanings of the colors and θ are stated in Fig. 3 and Fig. S1.

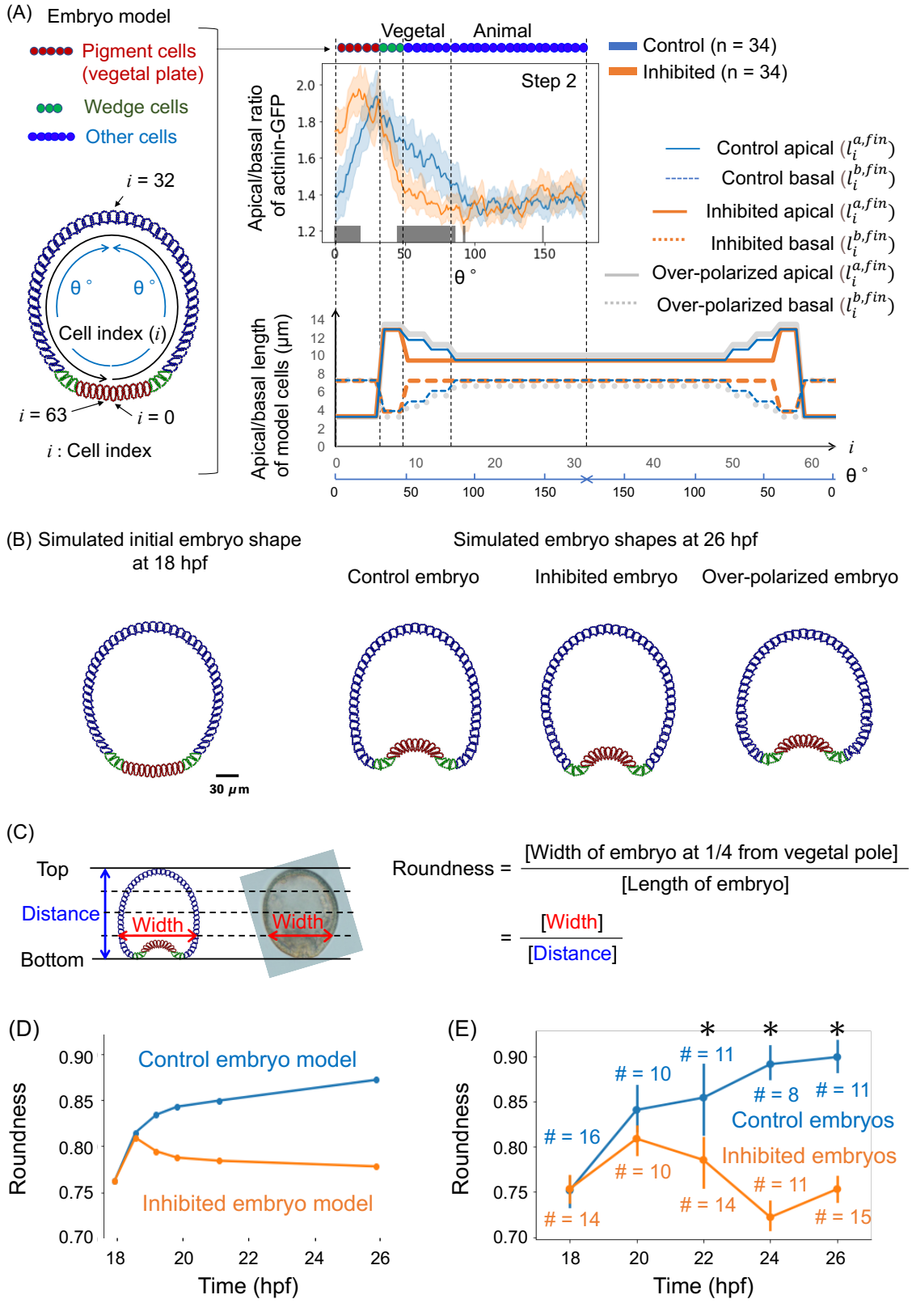

Fig. 5. Coarse-grained model and simulation of control, inhibited, and over-

742 **polarized embryos.** (A) Modeled cell lengths of apical and basal sides of control,
743 inhibited, and over-polarized embryos; $l_i^{a,fin}$ and $l_i^{b,fin}$ refer to the final length of the
744 apical and basal sides of the *i*-th cell, respectively (see Materials and methods).
745 Distributions of the final length of the former two models was determined based on the
746 distributions of apical/basal ratios of actinin-GFP intensities from control and inhibited
747 embryos in step 2. The top center panel was a modification of Fig. 3D. Red, green, and
748 blue circles in the top panel and panel (B) represent pigment cells, wedge cells, and
749 other cells, respectively. (B) Snapshots of the initial embryo shape at 18 hpf and at 26
750 hpf of the three models. (C) Definition of the roundness of the vegetal side of embryos
751 from simulation results and imaging. (D-E) Roundness indices of vegetal sides of
752 modeled control and inhibited embryos (D) and experimentally determined values (E).
753 Blue and orange # refer to the number of control and inhibited embryos at each time
754 point, error bars indicated 95% confidence intervals, and * indicated that the roundness
755 of control embryos was significantly larger than that of inhibited embryos according to
756 Welch's t-test ($p < 0.05$, see Fig. S4B).